Towards Determining Amyloid Fibril Structures Using Experimental Constraints from Raman Spectroscopy

Supporting Information

Madeline Harper[1], Uma Nudurupati[1], Riley J. Workman[2],

Taras I. Lakoba[3], Nicholas Perez[1], Delaney Nelson[1],

Yangguang Ou[1], and David Punihaole[*,1]

[1]Department of Chemistry, University of Vermont, Burlington, Vermont 05405, United States

[2]Sealy Center for Structural Biology and Molecular Biophysics,

University of Texas Medical Branch, Galveston, Texas 77555, United States

[3]Department of Mathematics and Statistics,

University of Vermont, Burlington, VT 05405, United States

[*]Email: David.Punihaole@uvm.edu

Raman spectra of sample mapping. To ensure that the set of polarized data were representative of the whole sample for all polymorphs, spectra were taken in 1 µm steps along the edge of the coffee ring. As shown in Figure S9, the spectra are highly reproducible, indicating that the peptide film is highly homogeneous in the region that was spectroscopically interrogated.

Raman spectroscopy of Isotropic samples. To determine $\langle P_2 \rangle$ and $\langle P_4 \rangle$, R_{iso} must also be calculated from an isotropic sample (see below). The original lyophilized peptide powder of amylin$_{20-29}$ and Aβ_{25-35} is a good representation of an isotropic sample, as there is no orientation preference. Because of this, $I_{ZZ} = I_{XX}$ and $I_{ZX} = I_{XZ}$ (Figure S10).

Spectral Processing. The measured Raman spectra were processed and peak-resolved using home-written MATLAB scripts described previously by Mustafa *et al.*[1] The spectra were first preprocessed by removing cosmic rays before averaging. The averaged spectra were calibrated against the 1266.4 and 1444.4 cm^{-1} bands of cyclohexane. In some cases, spectra needed to be additionally baseline-corrected due to a fluorescence background (Figure S11). All spectral analysis (see below) was performed on the original and not smoothed spectra.

Peak Fitting of Raman Spectra. We used a home-written program in MATLAB to peak fit the Raman spectra, $S(\tilde{\nu})$, shown in Figures S4, S5, and S12 - S17 as a sum of n mixed Gaussian ($G(\tilde{\nu})$) and Lorentzian ($L(\tilde{\nu})$) bands:

$$S(\tilde{\nu}) = \sum_{i}^{n} f_i G_i(\tilde{\nu}) + (1 - f_i) L_i(\tilde{\nu}) \tag{S1}$$

$$G_i(\tilde{\nu}) = H_i e^{-\left(\frac{\tilde{\nu}-\tilde{\nu}_i}{w_i}\right)^2 (4 \ln (2))} \tag{S2}$$

$$L_i(\tilde{\nu}) = \frac{H_i}{4(\frac{\tilde{\nu}-\tilde{\nu}_i}{w_i})^2 + 1} \tag{S3}$$

where H_i, $\tilde{\nu}_i$, and w_i are the heights, center frequencies, and widths, respectively, of the ith Gaussian-Lorentzian band. The parameter f_i in eq. S1 is the fraction of Gaussian character of the ith band. If $f_i = 1$ the band is a pure Gaussian, whereas if $f_i = 0$ it is a pure Lorentzian.

We parsimoniously fit the spectra as the minimum sum of Gaussian and Lorentzian bands that could satisfactorily model the data and be physically assigned to a vibrational mode. The goodness-of-fit was assessed by examining the residuals, as well as the reduced χ^2-statistic (χ^2_{red}), which we estimated using the following equation:

$$\chi^2_{red} = \frac{1}{df} \sum_i \frac{(O_i - C_i)^2}{\sigma_i^2} \tag{S4}$$

where O_i and C_i are the experimentally measured and modeled data points, respectively. The degrees of freedom ($df = n - m$) equals the number of experimentally measured data points (n) minus the number of fit parameters (m). The variance (σ_i^2) was estimated by first smoothing the experimental data using a Savitzky-Golay filter.[2] After this, the smoothed spectrum was subtracted from the experimental spectrum and the variance was calculated from the residuals. An ideal fit is suggested if $\chi^2_{red} = 1$, whereas the data may be over parameterized if $\chi^2_{red} < 1$.

Determination of Ramachandran ψ-angle Distributions. The ψ-angle distributions shown in Figure 3 of the main text were determined using the approach described in detail by Asher and coworkers.[3] Briefly, we assume that the inhomogeneously broadened, experimentally measured Amide III$_3$ band profiles, $B(\tilde{\nu})$, can be decomposed into the sum of n

Lorentzian bands:

$$B(\tilde{\nu}) = \sum_{i}^{n} \frac{P_i \Gamma^2}{\Gamma^2 + (\tilde{\nu} - \tilde{\nu}_i)^2} \tag{S5}$$

where P_i is the probability of the i^{th} band to occur at center frequency $\tilde{\nu}_i$. The parameter Γ is the homogeneous linewidth of the Amide III_3 vibration, which is estimated to be ca. $7.5\,\mathrm{cm}^{-1}$ from experimental measurements.[3]

After decomposing the Amide III_3 band envelope into a sum of Lorentzian bands, we then correlated the different $\tilde{\nu}_i$ frequencies to their respective ψ-angles using the following equation:

$$\tilde{\nu}(\psi) = 1239\,\mathrm{cm}^{-1} - 54\ \mathrm{cm}^{-1} \sin(\psi + 26^\circ) \tag{S6}$$

The Amide III_3 band's frequency dependence on the Ramanchandran ψ-angle depends on the hydrogen bonding interactions of the peptide bond amide groups. Eq. S6 is a semi-empirical relationship that correlates the Amide III_3 band frequencies to ψ-angles for situations were peptide-peptide hydrogen bonding dominants over peptide-water hydrogen bonding. This equation has been successfully used to determine Ramanchandran ψ-angle distributions of fibrils by Lednev and coworkers[4] and Punihaole *et al.*[5,6]

Fourier-Transform Infrared (FTIR) Spectroscopy. FTIR spectra were acquired using an INVENIO® R (Bruker) equipped with an attenuated total reflection (ATR) unit. $Amylin_{20-29}$ polymorph 1 fibril solution was concentrated into a pellet after centrifugation and an aliquot was deposited onto the ATR diamond crystal. The aggregated solution was then dried with N_2 gas to create a film. The FTIR measurement was acquired using 72 scans at a 10 kHz scan rate with $0.5\,\mathrm{cm}^{-1}$ resolution (Figure S6).

Atomic Force Microscopy (AFM).

Additional AFM images for each polymorph are shown in Figure S2. All images in Figure

S2 were collected using the Asylum MFP-3D-BIO AFM instrument (Oxford Instruments) in the AC mode using standard AFM probe (PPP-NCHR, Nanosensors™) with a $42\,\mathrm{N\,m^{-1}}$ force constant and 330 Hz resonance frequency.

For amylin$_{20-29}$ polymorph 1, Figure S2a is a 512 line image of $1.7\,\mu\mathrm{m} \times 1.7\,\mu\mathrm{m}$ size and S2b is a 256 line image of $20\,\mu\mathrm{m} \times 20\,\mu\mathrm{m}$ size. For amylin$_{20-29}$ polymorph 2, Figures S2c and d are 512 line images of $10\,\mu\mathrm{m} \times 10\,\mu\mathrm{m}$ size. For Aβ_{25-35} fibrils, S2e is a 512 line image of $10\,\mu\mathrm{m} \times 10\,\mu\mathrm{m}$ image and Figure S2f is a 256 line image of $20\,\mu\mathrm{m} \times 20\,\mu\mathrm{m}$ size. All images were measured in AC mode.

Calculation of Order Parameters and Orientation Distribution Function.

Basic Approach to Determine the Most Probable Orientation Distribution Function. The aligned fibrils exhibit uniaxial symmetry, and therefore the distribution function, $N(\theta)$, of the angle θ which the fibrils make with the laboratory (polar) axis, has the symmetry property:

$$N(\pi - \theta) = N(\theta)\,. \tag{S7}$$

This distribution function can be approximated from the following constrained minimization approach.

On one hand, $N(\theta)$ is to maximize the information entropy[7–9]

$$S[N(\theta)] = -\int_0^{\pi} N(\theta)\,\ln N(\theta)\,\sin\theta\,d\theta \;\equiv\; \int_{\cos\theta=-1}^{\cos\theta=1} N(\cos\theta)\,\ln N(\cos\theta)\,d\cos\theta\,. \tag{S8}$$

Here the factor $\sin\theta$ is the standard conversion factor from Cartesian to spherical coordinates, which are the appropriate coordinates in problems involving a polar axis. On the other hand, $N(\theta)$ must satisfy a number of constraints, the first of which is unitary normalization:

$$\int_0^{\pi} N(\theta)\,\sin\theta\,d\theta = 1\,. \tag{S9}$$

The other constraints are dictated by the fact that $N(\theta)$ must correctly predict the measured values of so-called order parameters $\langle P_2 \rangle$ and $\langle P_4 \rangle$, where $P_2(\theta)$ and $P_4(\theta)$ are the Legendre polynomials of respective orders:[9,10]

$$P_2(\theta) = \frac{1}{2}(3\cos^2\theta - 1)\,, \tag{S10}$$

$$P_4(\theta) = \frac{1}{8}(35\cos^4\theta - 30\cos^2\theta + 3)\,, \tag{S11}$$

and the angle brackets stand for the averaging over all fibril orientations. For self-consistency, this averaging must be done with the distribution function $N(\theta)$:

$$\langle P_j \rangle = \int_0^\pi P_j(\cos\theta)\, N(\theta)\, \sin\theta\, d\theta\,, \qquad j = 2, 4. \tag{S12}$$

The measurement of $\langle P_2 \rangle$ and $\langle P_4 \rangle$ is described in the next subsection. Note that symmetry in eq. S7 ensures that the averages of odd-order Legendre polynomials, which are expressed in terms of only odd degrees of $\cos\theta$, vanish; i.e., $\langle \cos^\ell \theta \rangle = 0$ for all odd ℓ.

A distribution function maximizing the information entropy in eq. S8 subject to the constraints of eqs. S9, S12 (where $\langle P_2 \rangle$ and $\langle P_4 \rangle$ are considered known from the measurements) is found via the standard approach using Lagrange multipliers, λ_2 and λ_4, and has the form:[9]

$$N_{mp}(\theta) = \frac{e^{\lambda_2 \cdot P_2(\cos\theta) + \lambda_4 \cdot P_4(\cos\theta)}}{\int_0^\pi e^{\lambda_2 \cdot P_2(\cos\theta) + \lambda_4 \cdot P_4(\cos\theta)} \cdot \sin(\theta) d\theta} \tag{S13}$$

Here the subscript "mp" reflects the fact that this $N_{mp}(\theta)$ results in the most probable measured values of $\langle P_2 \rangle$ and $\langle P_4 \rangle$. (The Lagrange multiplier λ_0 corresponding to the constraint S9 is just the denominator in S13.) The Lagrange multipliers λ_2 and λ_4 are calculated by substituting eq. S13 into S12. This yields two nonlinear equations for these parameters, which we solved by a MATLAB code. Substituting their values back into S13 yields the most probable distribution function $N_{mp}(\theta)$.

Determining $\langle P_2 \rangle$ and $\langle P_4 \rangle$ from Polarized Raman Spectra. Polarized Raman spectroscopy can be used to measure $\langle P_2 \rangle$ and $\langle P_4 \rangle$, which, in turn, are needed to determine $N_{mp}(\theta)$ for the Raman tensors of the Amide I $A(0,0)$ modes. As described in detail elsewhere,[11] $\langle P_2 \rangle$ and $\langle P_4 \rangle$ can be determined from the intensity ratios, R_1 and R_2. For fibrils possessing uniaxial symmetry, R_1 and R_2 are equal to:

$$R_1 = \frac{I_{ZX}}{I_{ZZ}} = \frac{A\langle(\alpha_{ZX})^2\rangle + B\langle(\alpha_{ZY})^2\rangle}{A\langle(\alpha_{ZZ})^2\rangle + B\langle(\alpha_{ZY})^2\rangle} \tag{S14}$$

$$R_2 = \frac{I_{XZ}}{I_{XX}} = \frac{A\langle(\alpha_{XZ})^2\rangle + B\langle(\alpha_{XY})^2\rangle}{A\langle(\alpha_{XX})^2\rangle + B\langle(\alpha_{XY})^2\rangle} \tag{S15}$$

where I_{ZX}, I_{ZZ}, I_{XZ}, and I_{XX} are the intensities of the Amide I $A(0,0)$ vibrational mode corresponding to each measurement (See Experimental Methods section titled *Raman Spectroscopy*). $\langle \alpha_{ZX} \rangle$, $\langle \alpha_{ZY} \rangle$, $\langle \alpha_{ZZ} \rangle$, and $\langle \alpha_{XX} \rangle$ are $\langle \alpha_{ij} \rangle$ averages related to the principle component of a Raman tensor with uniaxial symmetry.[11] A and B correct for the scrambling of the polarization for the incident and scattered light in the focal plane due to the use of a high numerical aperture ($NA = 0.9$) microscope objective. These correction factors can be determined by considering the effective half-angle (θ_m) of the solid angle of light collection inside the sample using the following expressions:

$$A = \pi^2 \left(\frac{4}{3} - \cos\theta_m - \frac{1}{3}\cos^3\theta_m \right) \tag{S16}$$

$$B = 2\pi^2 \left(\frac{2}{3} - \cos\theta_m - \frac{1}{3}\cos^3\theta_m \right) \tag{S17}$$

$$\theta_m = \sin^{-1}\left(\frac{NA}{n}\right) \tag{S18}$$

where $n = 1.55$ is the refractive index of the sample.[12] The values of R_1, R_2, $\langle P_2 \rangle$, $\langle P_4 \rangle$, λ_2, and λ_4 needed to determine $N_{mp}(\theta)$ for the Amide I $A(0,0)$ tensors are summarized in Table S1 and S2.

Table S1: Amide I $A(0,0)$ orientation distribution parameters for amylin$_{20-29}$ fibrils

	Mode	R_1	R_2	$\langle P_2 \rangle$	$\langle P_4 \rangle$	λ_2	λ_4	R_{iso}	a
Polymorph 1	Amide I $A(0,0)$	0.11 ± 0.0023	0.57 ± 0.018	0.50	0.50	0.75	3.04	0.52 ± 0.0070	-0.12
Polymorph 2	Amide I $A(0,0)$	0.19 ± 0.0030	0.77 ± 0.062	0.41	0.28	1.21	1.33	0.52 ± 0.0070	-0.12

Table S2: Amide I $A(0,0)$ orientation distribution parameters for Aβ_{25-35} fibrils

Mode	R_1	R_2	$\langle P_2 \rangle$	$\langle P_4 \rangle$	λ_2	λ_4	R_{iso}	a
Amide I $A(0,0)$	0.24 ± 0.0050	0.54 ± 0.011	0.29	0.40	0.28	2.83	0.70 ± 0.013	-0.29

Table S3: Inter-sheet and inter-strand spacing for amylin$_{20-29}$ and Aβ_{25-35} fibrils from MD simulations

	Inter-sheet spacing (Å)	Inter-strand spacing (Å)
Amylin$_{20-29}$ polymorph 1	10.4 ± 0.1Å	5.0 ± 0.1Å
Amylin$_{20-29}$ polymorph 2	9.5 ± 0.2Å	4.9 ± 0.1Å
Aβ_{25-35} fibrils	9.4 ± 0.1Å	5.1 ± 0.1Å

Table S4: Residue-specific mean Ramachandran angles (in degrees) predicted for amylin$_{20-29}$ polymorph 1 fibrils from constrained MD simulations

Residue	ψ	ϕ	$\lvert\omega\rvert^a$
Ser20	–	–	173.1 ± 5.3
Asn21	$+140.3 \pm 11.7$	-126.9 ± 15.0	173.4 ± 5.2
Asn22	$+136.5 \pm 12.3$	-138.6 ± 12.3	173.4 ± 5.0
Phe23	$+138.0 \pm 16.9$	-133.1 ± 12.8	172.1 ± 5.9
Gly24	$+139.1 \pm 58.4$	-119.5 ± 86.2	173.2 ± 5.1
Ala25	$+145.6 \pm 10.6$	-147.2 ± 13.0	174.1 ± 4.6
Ile26	$+133.5 \pm 10.9$	-125.0 ± 10.9	173.2 ± 5.0
Leu27	$+134.6 \pm 13.0$	-129.3 ± 13.8	173.1 ± 5.3
Ser28	$+138.9 \pm 13.2$	-137.8 ± 13.4	172.7 ± 5.4
Ser29	–	–	–

[a] ω values are absolute values.

Table S5: Residue-specific mean Ramachandran angles (in degrees) predicted for amylin$_{20-29}$ polymorph 2 fibrils from constrained MD simulations

Residue	ψ	ϕ	$\lvert\omega\rvert^a$
Ser20	–	–	172.7 ± 5.6
Asn21	$+131.0 \pm 11.3$	-117.3 ± 19.3	172.7 ± 5.5
Asn22	$+130.1 \pm 11.1$	-126.8 ± 12.5	173.3 ± 5.0
Phe23	$+129.5 \pm 11.2$	-125.9 ± 11.9	172.8 ± 5.2
Gly24	$+128.8 \pm 16.4$	-124.4 ± 24.1	173.5 ± 5.0
Ala25	$+128.6 \pm 12.7$	-124.9 ± 17.1	172.8 ± 5.3
Ile26	$+128.4 \pm 10.1$	-121.3 ± 10.1	172.8 ± 5.2
Leu27	$+130.5 \pm 10.8$	-127.9 ± 14.3	171.0 ± 6.3
Ser28	$+128.6 \pm 14.3$	-128.6 ± 24.0	172.8 ± 5.2
Ser29	–	–	–

[a] ω values are absolute values.

Table S6: Residue-specific mean Ramachandran angles (in degrees) predicted for Aβ_{25-35} fibrils from constrained MD simulations

Residue	ψ	ϕ	$\lvert\omega\rvert^a$
Gly25	–	–	172.9 ± 5.4
Ser26	$+137.3 \pm 10.9$	-106.4 ± 38.4	173.1 ± 5.4
Asn27	$+130.0 \pm 20.2$	-132.0 ± 16.1	172.4 ± 5.5
Lys28	$+137.8 \pm 12.8$	-136.9 ± 14.4	172.9 ± 5.4
Gly29	$+138.9 \pm 31.2$	-115.7 ± 81.5	172.6 ± 5.6
Ala30	$+130.6 \pm 13.1$	-131.8 ± 16.9	173.2 ± 5.3
Ile31	$+126.6 \pm 12.3$	-119.0 ± 10.6	171.9 ± 5.9
Ile32	$+134.2 \pm 15.2$	-130.3 ± 12.1	171.2 ± 6.3
Gly33	$+113.0 \pm 63.6$	-112.1 ± 76.9	172.9 ± 5.3
Leu34	$+90.6 \pm 51.0$	-115.9 ± 16.9	172.7 ± 5.5
Met35	–	–	–

[a] ω values are absolute values.

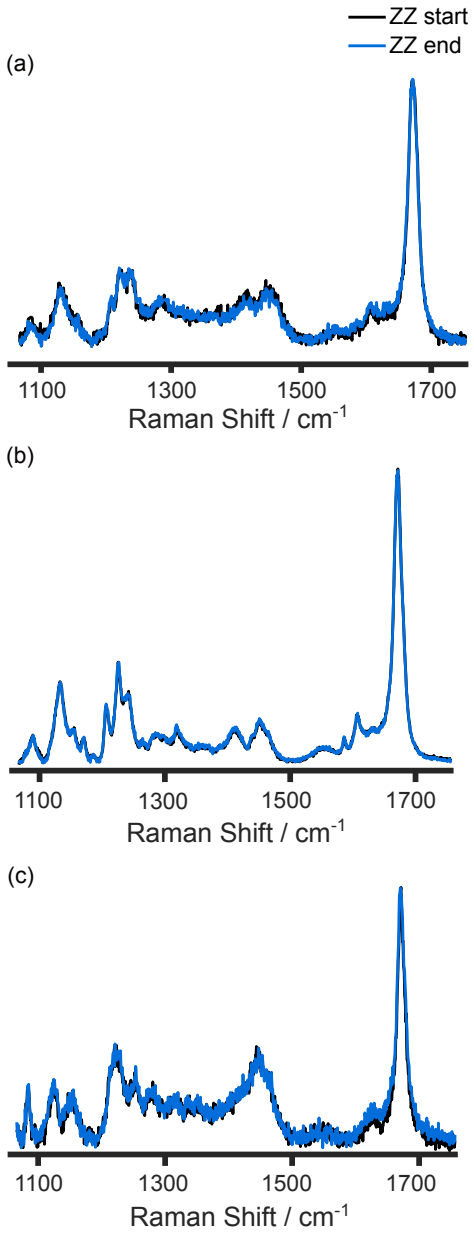

Figure S1: ZZ spectra at the beginning (ZZ start) and end (ZZ end) of the polarization measurements for (a) amylin$_{20-29}$ polymorph 1, (b) amylin$_{20-29}$ polymorph 2, and (c) Aβ_{25-35} polymorph 1. All spectra are normalized to the Amide I vibrational mode. The spectra overlap perfectly, indicating that the sample was not degraded by the laser light over the course of the measurements.

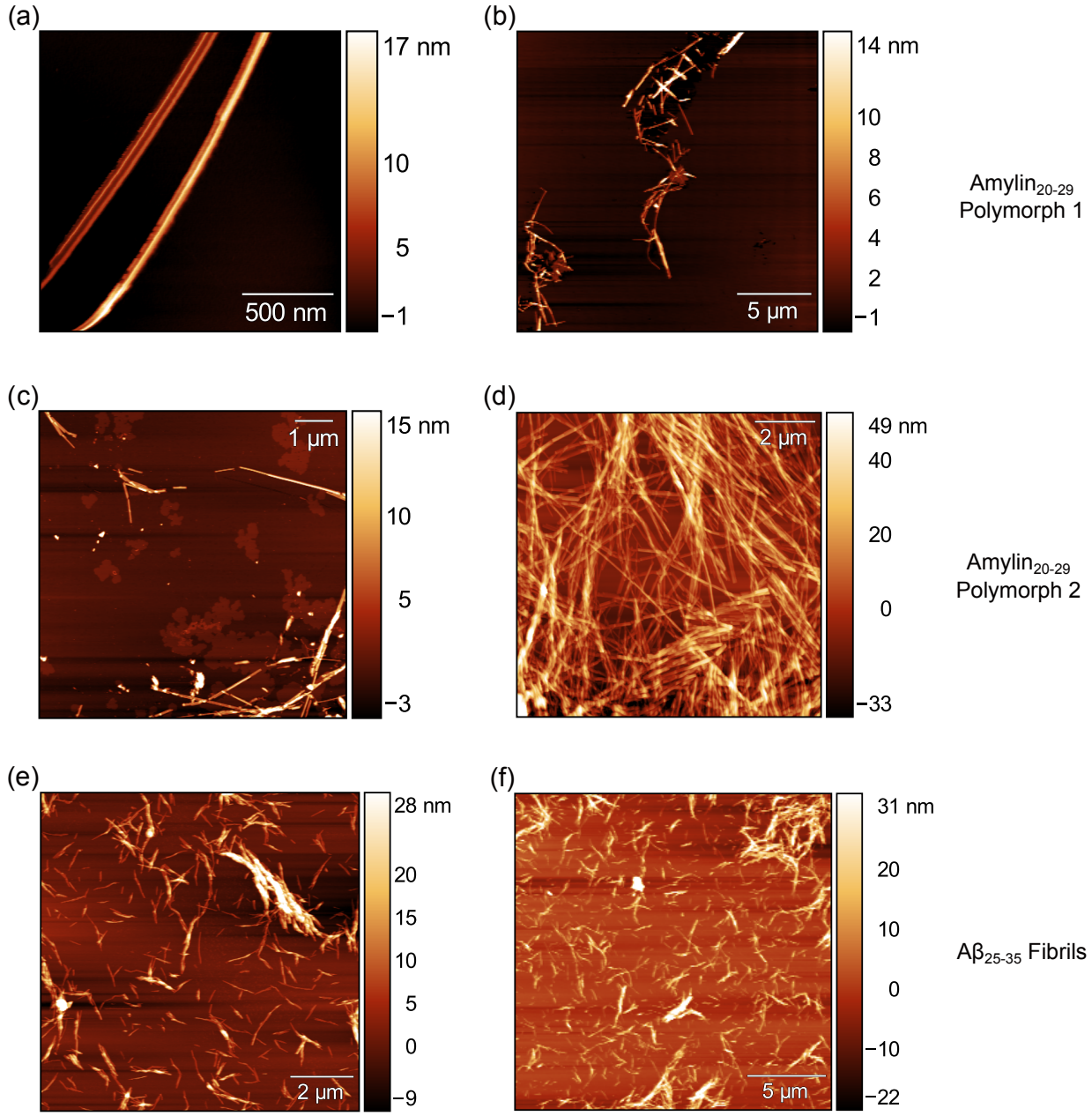

Figure S2: Additional AFM images of amylin$_{20-29}$ fibrils and Aβ_{25-35} fibrils. (a,b) AFM images of amylin$_{20-29}$ polymorph 1 ((a) 500 nm scalebar, (b) 5 µm scalebar). (c,d) AFM images of amylin$_{20-29}$ polymorph 2 ((c) 1 µm scalebar, (d) 2 µm scalebar). (e,f) AFM images of Aβ_{25-35} polymorph 1 ((e) 2 µm scalebar, (f) 5 µm scalebar). Note: Panel d is an adjacent region as Figure 1b in main text, but in a different location. All images were measured in AC mode.

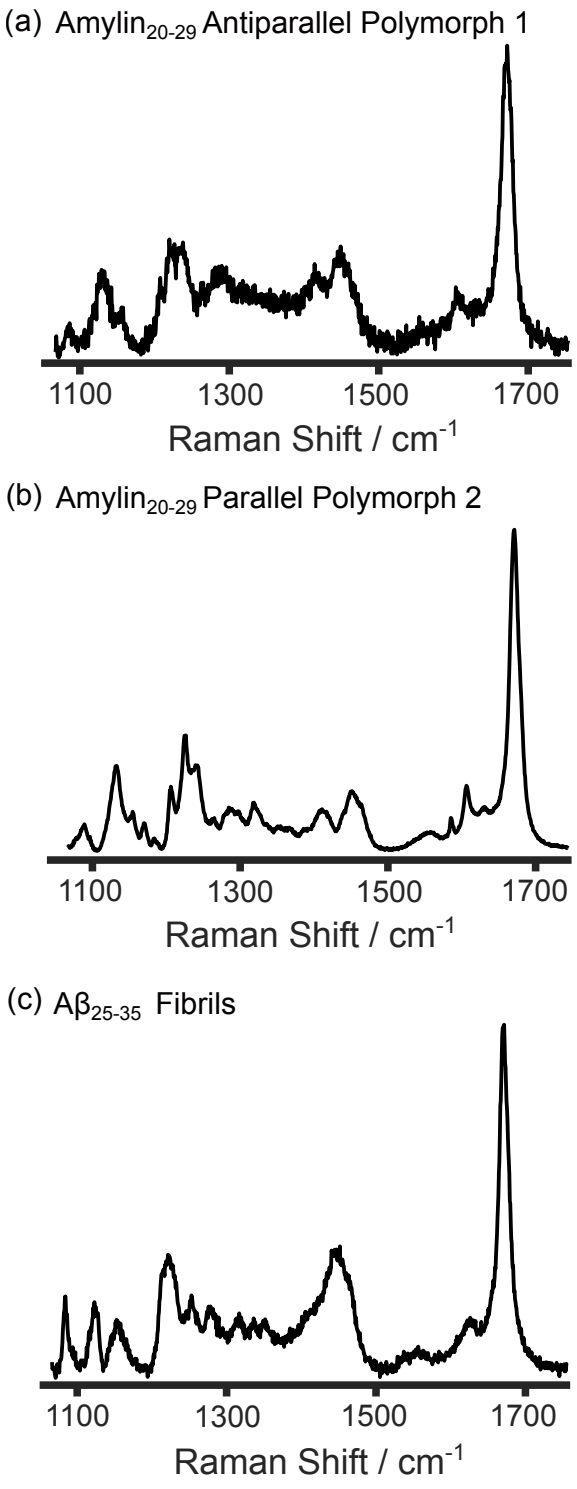

Figure S3: Non-polarized Raman spectra of (a) amylin$_{20-29}$ polymorph 1, (b) amylin$_{20-29}$ polymorph 2, and (c) Aβ_{25-35} fibrils.

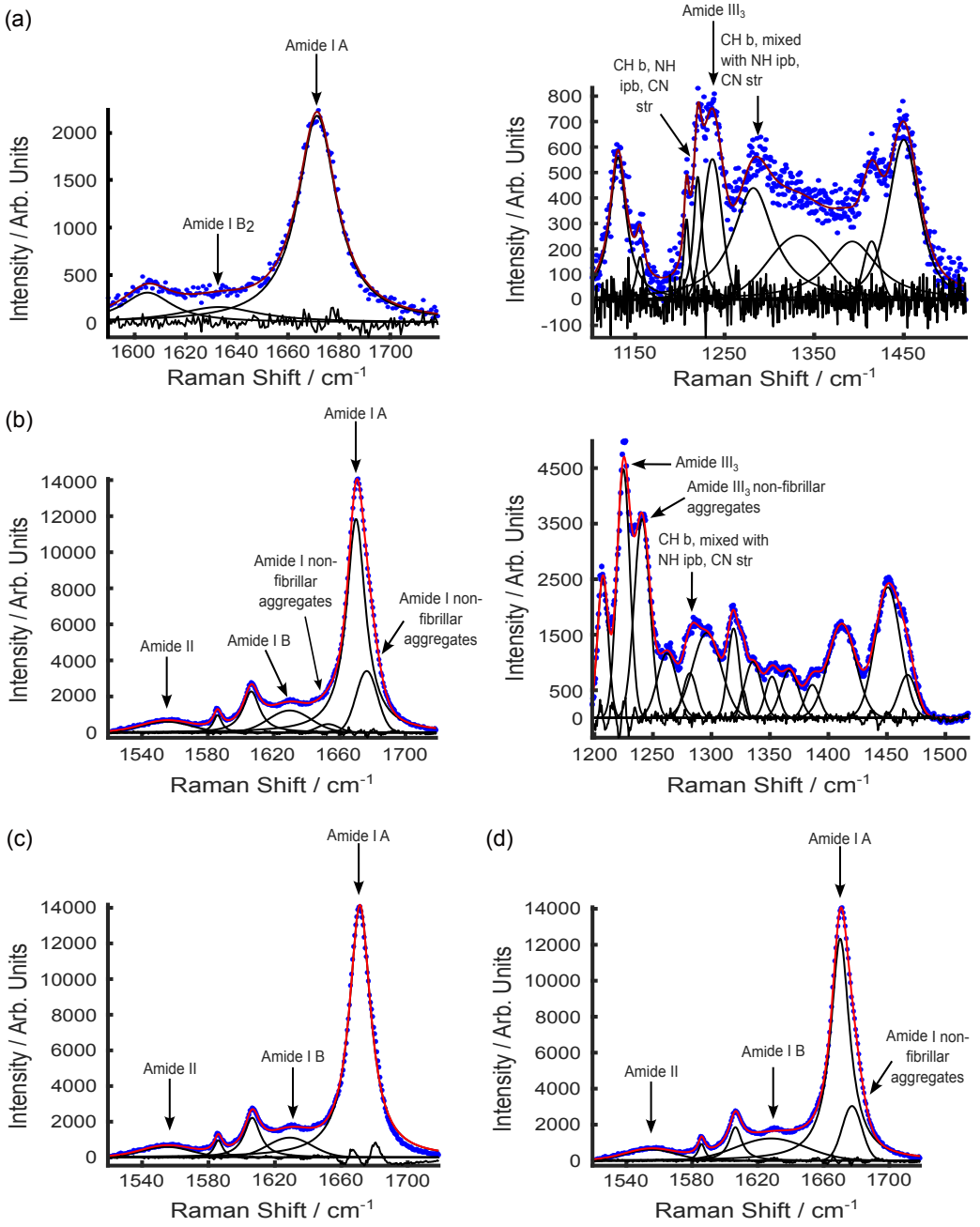

Figure S4: Deconvolution of amylin$_{20-29}$ fibril Raman spectra for the Amide I and Amide III regions. (a) Amylin$_{20-29}$ polymorph 1 Amide I ($\chi^2_{red} = 1.6$) and Amide III regions ($\chi^2_{red} = 1.2$). (b) Amylin$_{20-29}$ polymorph 2 Amide I ($\chi^2_{red} = 2.1$) and Amide III regions ($\chi^2_{red} = 3.0$). (c) Example of a poor fit of the Amide I region for amylin$_{20-29}$ polymorph 2 using only the Amide I A and B modes ($\chi^2_{red} = 16.6$). (d). Another example of a poor fit of the Amide I region for amylin$_{20-29}$ polymorph 2. Adding an additional band in the Amide I region still results in a poor fit since the Amide I B mode at 1628 cm^{-1} becomes unphysically large, $> 50\,\mathrm{cm}^{-1}$ ($\chi^2_{red} = 2.2$).

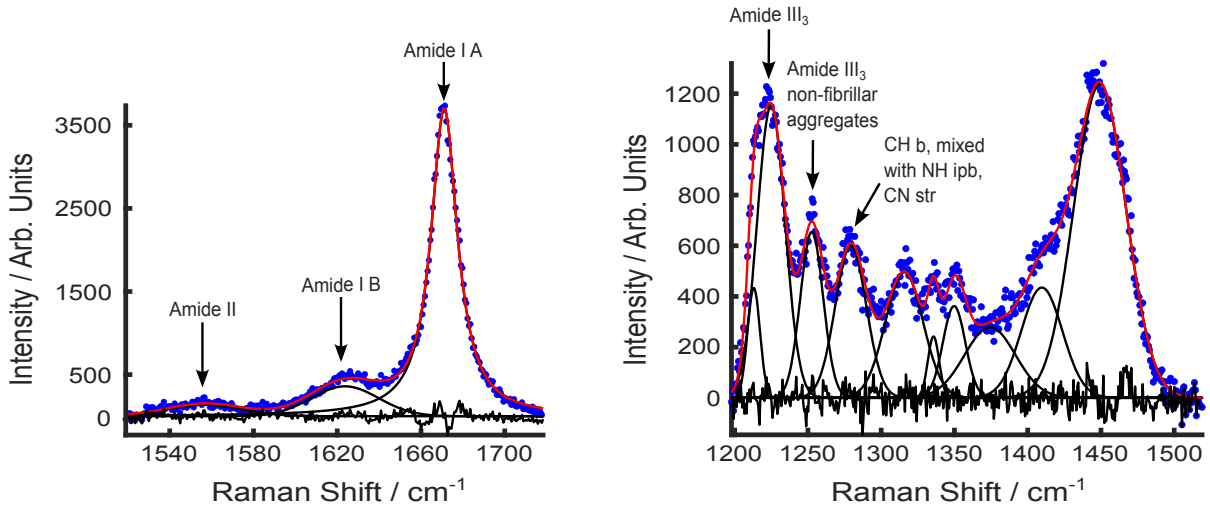

Figure S5: Deconvolution of Aβ_{25-35} fibril Raman spectra for the Amide I ($\chi^2_{red} = 2.6$) and Amide III regions ($\chi^2_{red} = 1.6$).

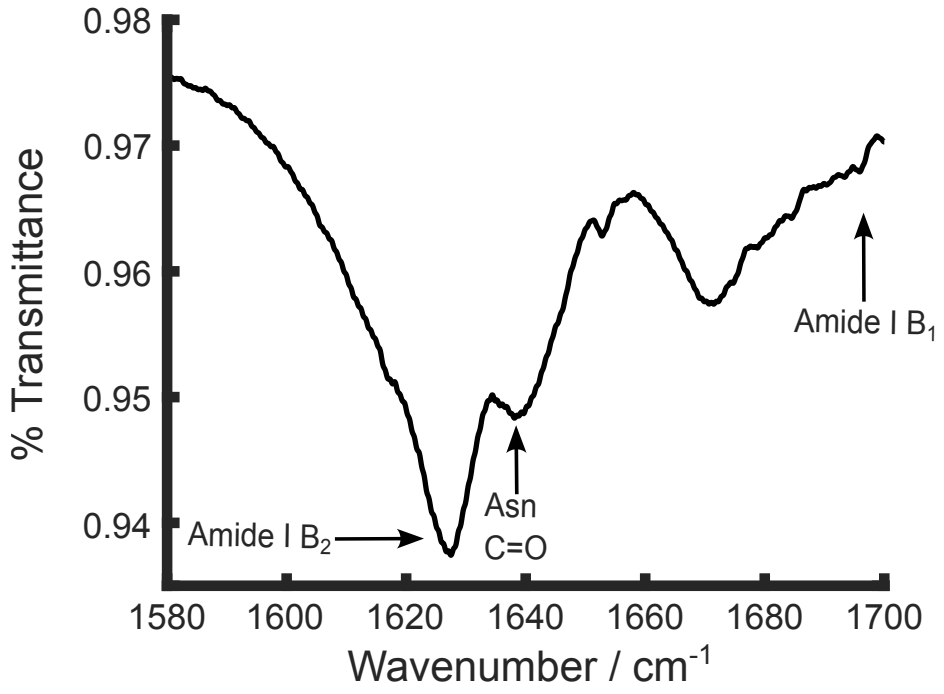

Figure S6: Amylin_{20-29} polymorph 1 FTIR spectrum smoothed with a Savitzky Golay filter[2] (2^{nd}-order, 25 point region).

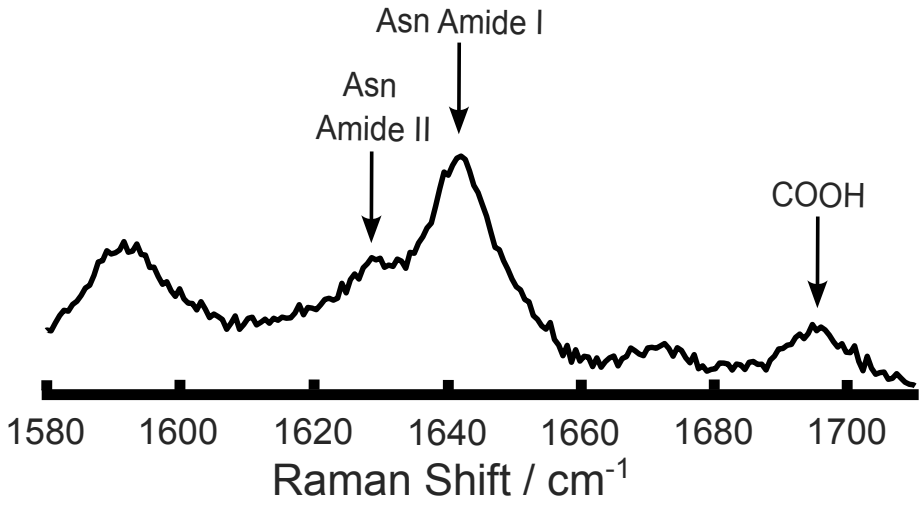

Figure S7: Raman spectrum of asparagine in the solid-state.

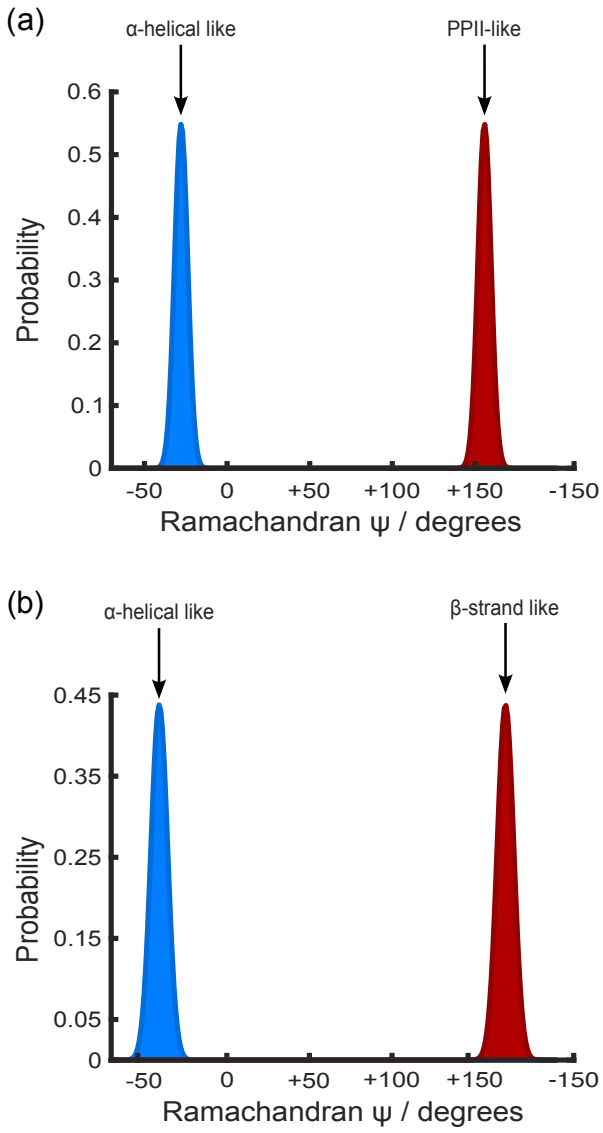

Figure S8: Ramachandran ψ-angle distribution determined from upshifted Amide III_3 vibrational modes. (a) $Amylin_{20-29}$ polymorph 2 Ramachandran ψ-angle distribution with a mean ψ-angle of -28° and 156°. (b) $A\beta_{25-35}$ polymorph 1 Ramachandran ψ-angle distribution with a mean ψ-angle of -40° and 168°.

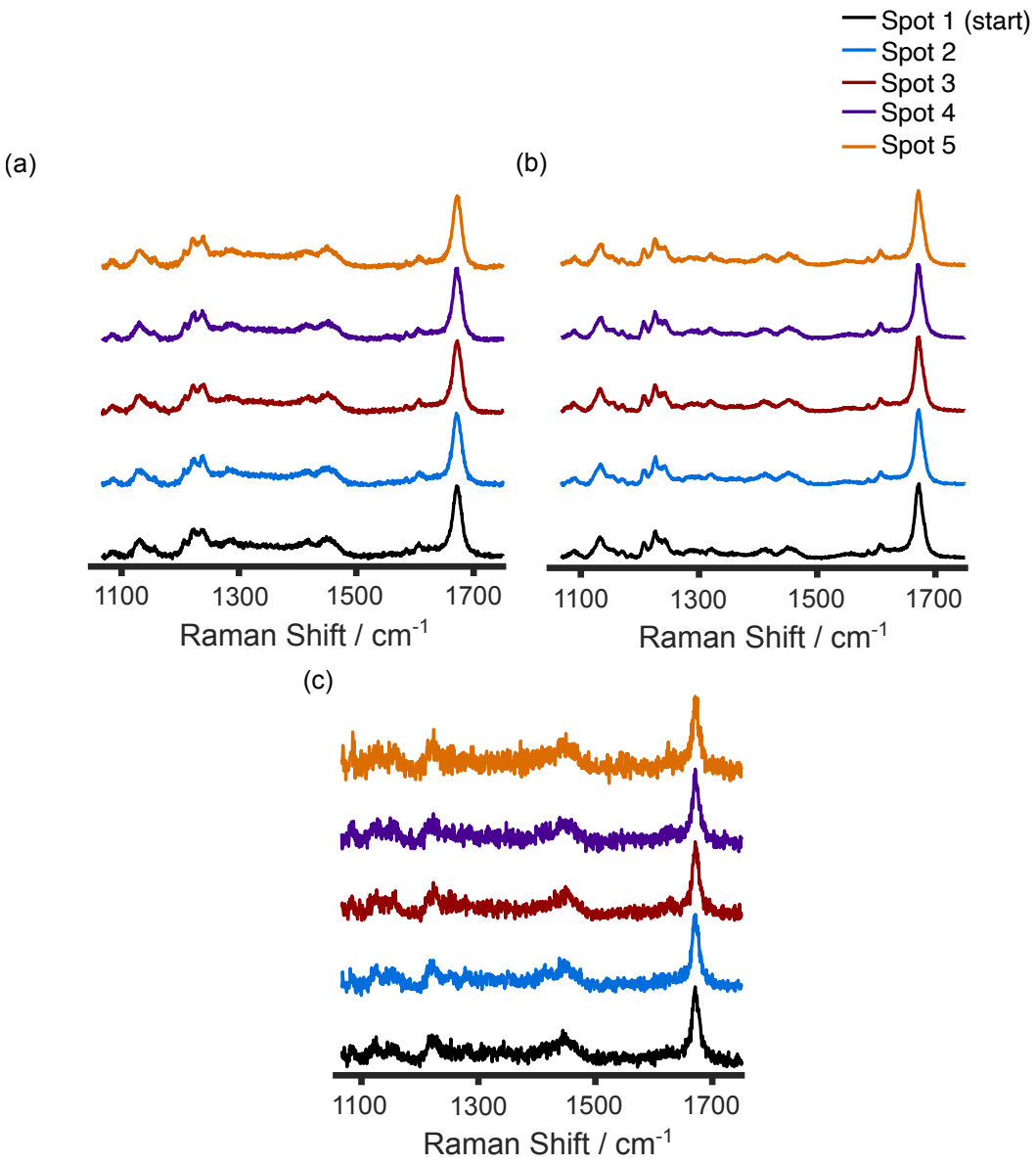

Figure S9: Amylin$_{20-29}$ and Aβ_{25-35} spectra measured in 1 µm increments along the sample. The spectra are highly reproducible, indicating the sample is homogeneous in the region that was interrogated. All spectra were normalized to the Amide I band intensity. All spectra are offset for visual clarity. (a) Amylin$_{20-29}$ polymorph 1. (b) Amylin$_{20-29}$ polymorph 2. (c) Aβ_{25-35} fibrils.

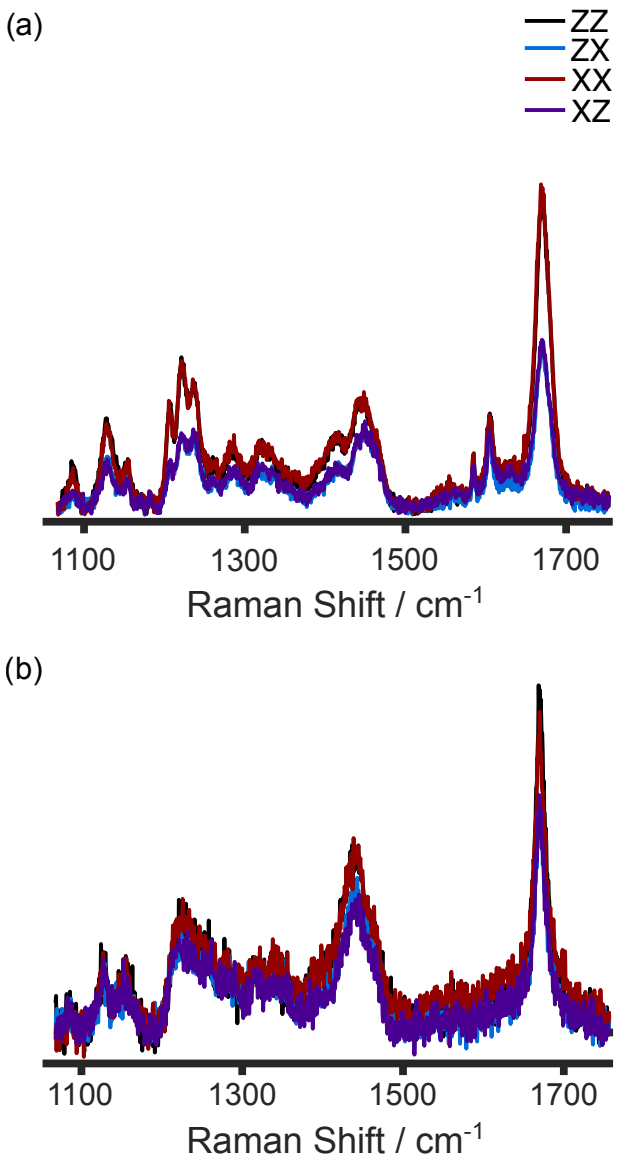

Figure S10: Isotropic powder spectra of all four incident/scattered light polarization configurations, ZZ, ZX, XX, and XZ for (a) amylin$_{20-29}$ and (b) Aβ_{25-35}. Each amylin$_{20-29}$ powder spectrum in (a) was acquired for 300 s while each Aβ_{25-35} powder spectrum in (b) was acquired for 150 s.

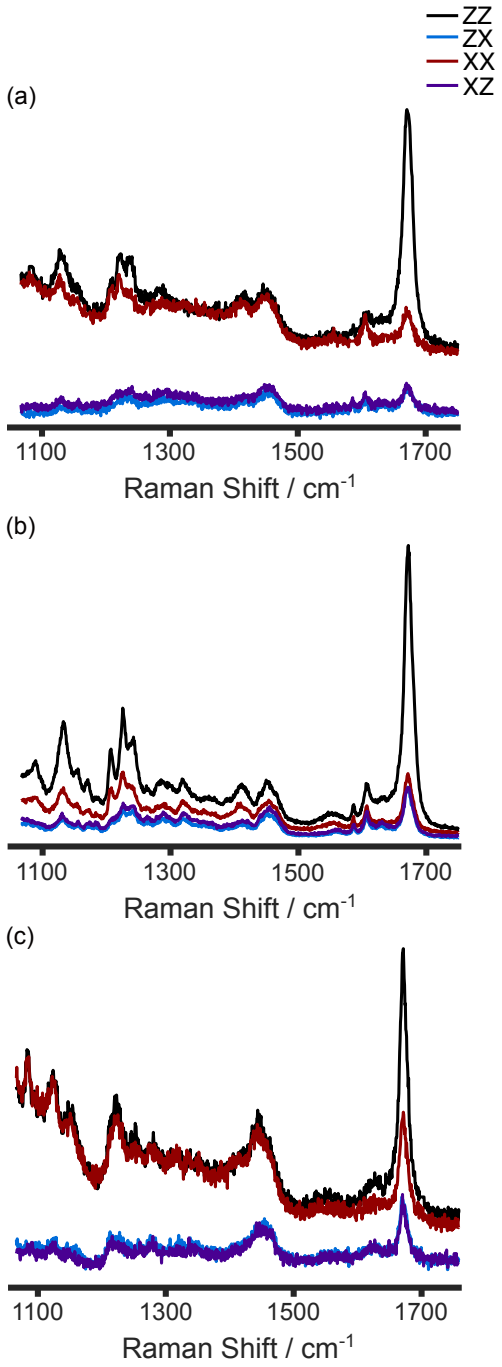

Figure S11: Amylin$_{20-29}$ and Aβ_{25-35} polarized Raman spectra of all four incident/scattered light polarization configurations, ZZ, ZX, XX, and XZ, prior to baseline processing. (a) Amylin$_{20-29}$ polymorph 1 fibrils. (b) Amylin$_{20-29}$ polymorph 2 fibrils. (c) Aβ_{25-35} fibrils.

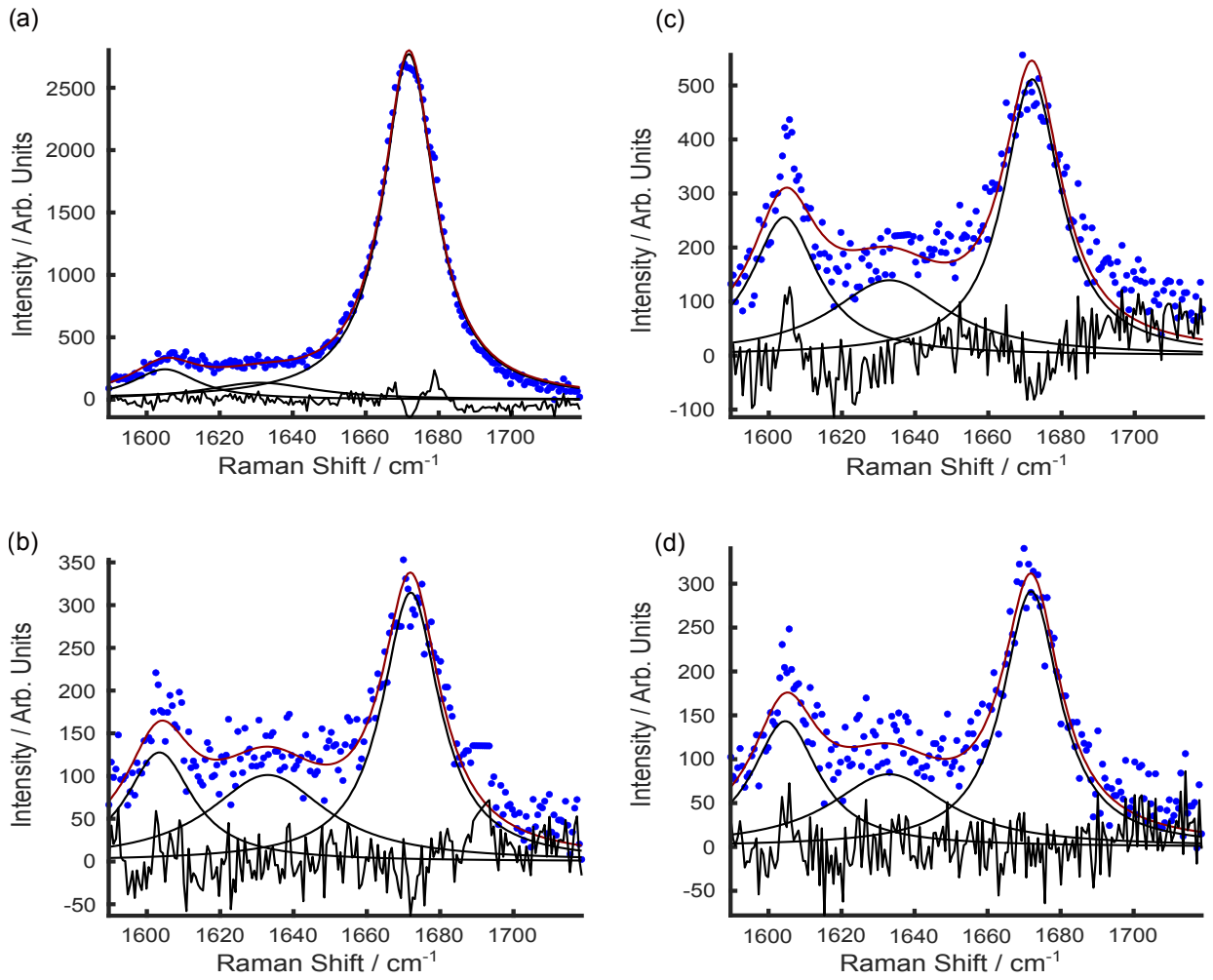

Figure S12: Deconvolution of amylin$_{20-29}$ polymorph 1 polarized Raman spectra for the Amide I region: (a) ZZ ($\chi^2_{red} = 3.6$), (b) ZX ($\chi^2_{red} = 1.9$), (c) XX ($\chi^2_{red} = 2.9$), and (d) XZ ($\chi^2_{red} = 1.9$)

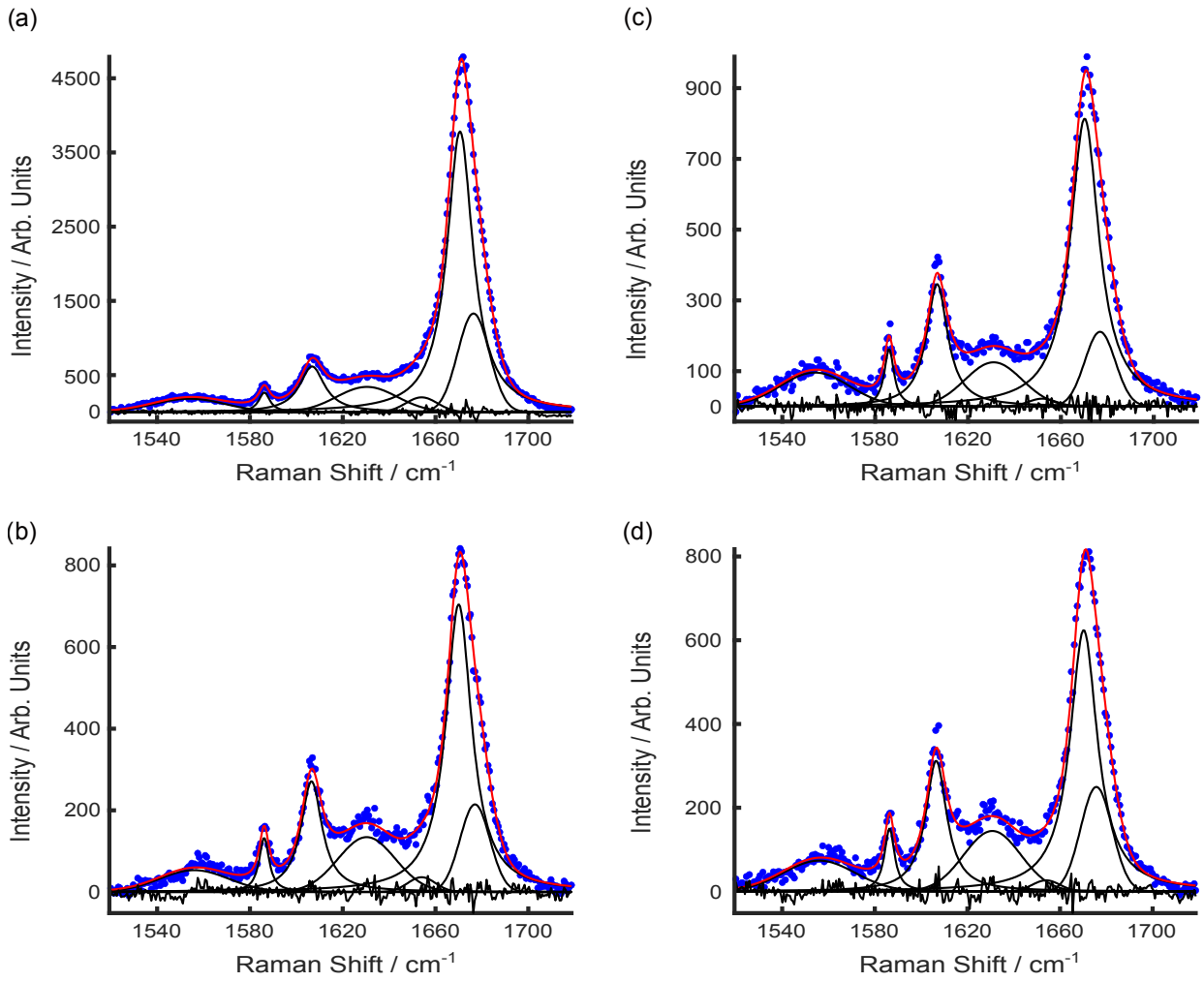

Figure S13: Deconvolution of amylin$_{20-29}$ polymorph 2 polarized Raman spectra for the Amide I region: (a) ZZ ($\chi^2_{red} = 1.8$), (b) ZX ($\chi^2_{red} = 1.5$), (c) XX ($\chi^2_{red} = 1.2$), and (d) XZ ($\chi^2_{red} = 1.6$).

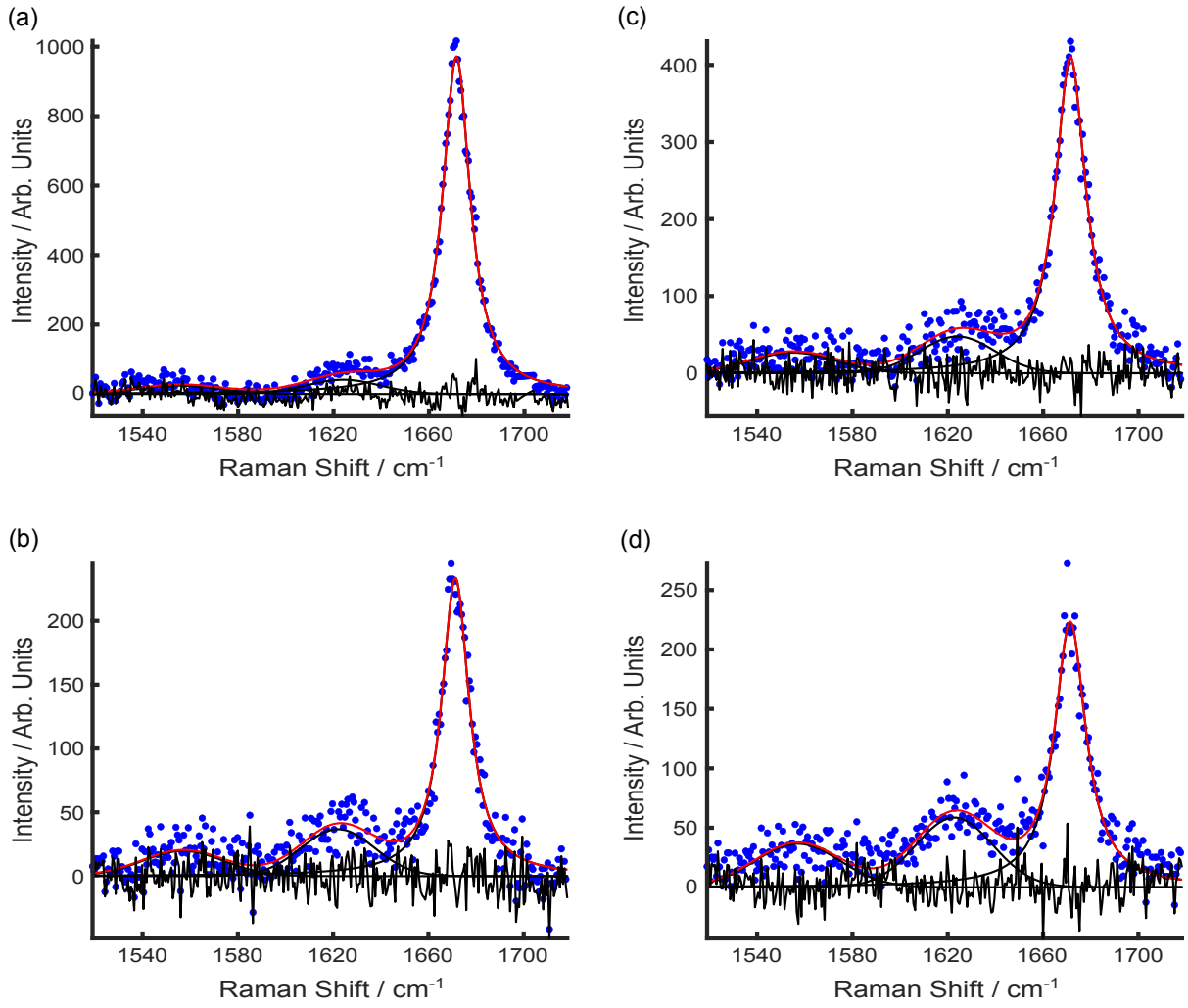

Figure S14: Deconvolution of Aβ_{25-35} fibrils polarized Raman spectra for the Amide I region: (a) ZZ ($\chi^2_{red} = 1.8$), (b) ZX ($\chi^2_{red} = 1.2$), (c) XX ($\chi^2_{red} = 1.2$), and (d) XZ ($\chi^2_{red} = 1.2$).

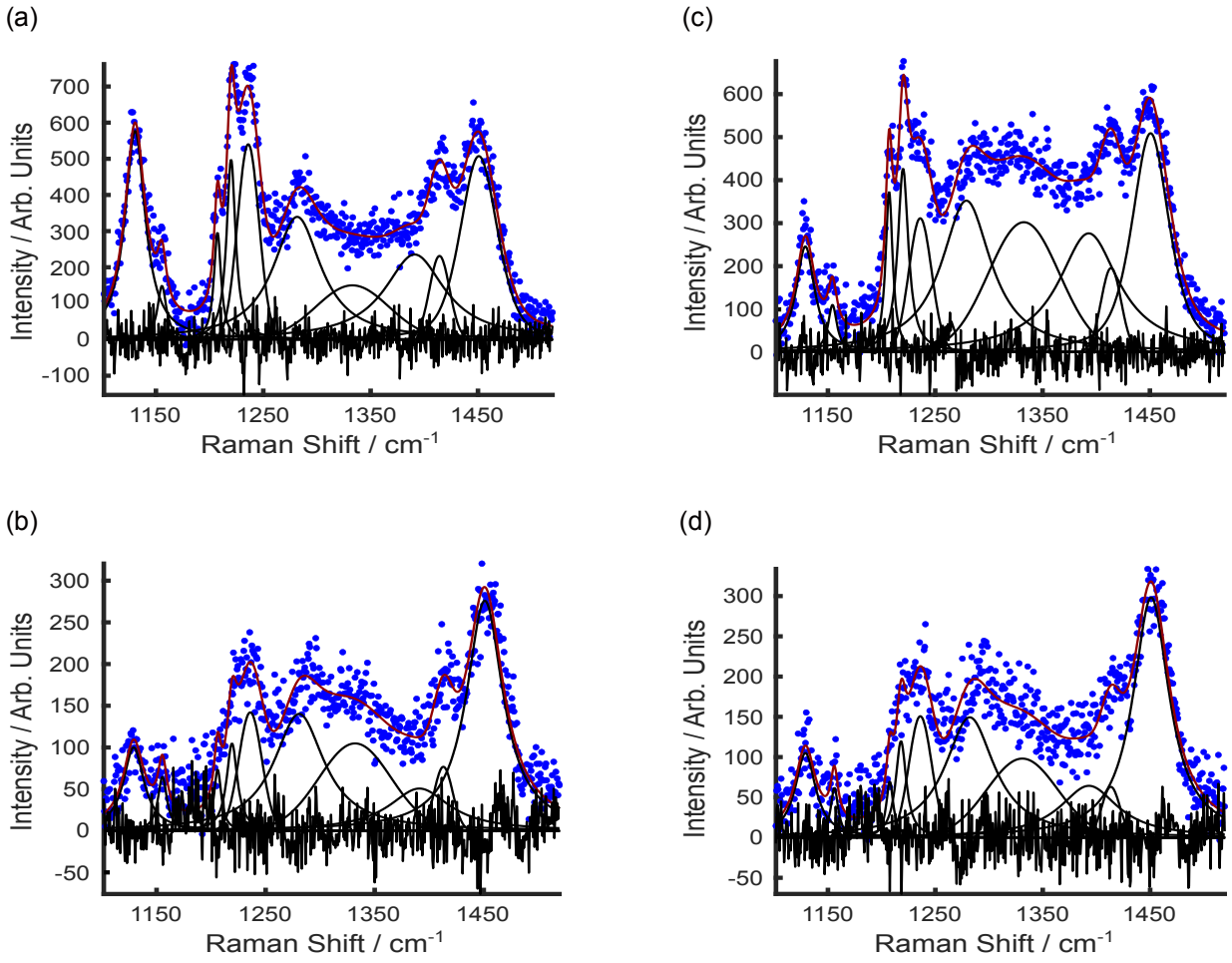

Figure S15: Deconvolution of amylin$_{20-29}$ polymorph 1 polarized Raman spectra for the Amide III region: (a) ZZ ($\chi^2_{red} = 1.3$), (b) ZX ($\chi^2_{red} = 1.5$), (c) XX ($\chi^2_{red} = 1.5$), and (d) XZ ($\chi^2_{red} = 1.4$).

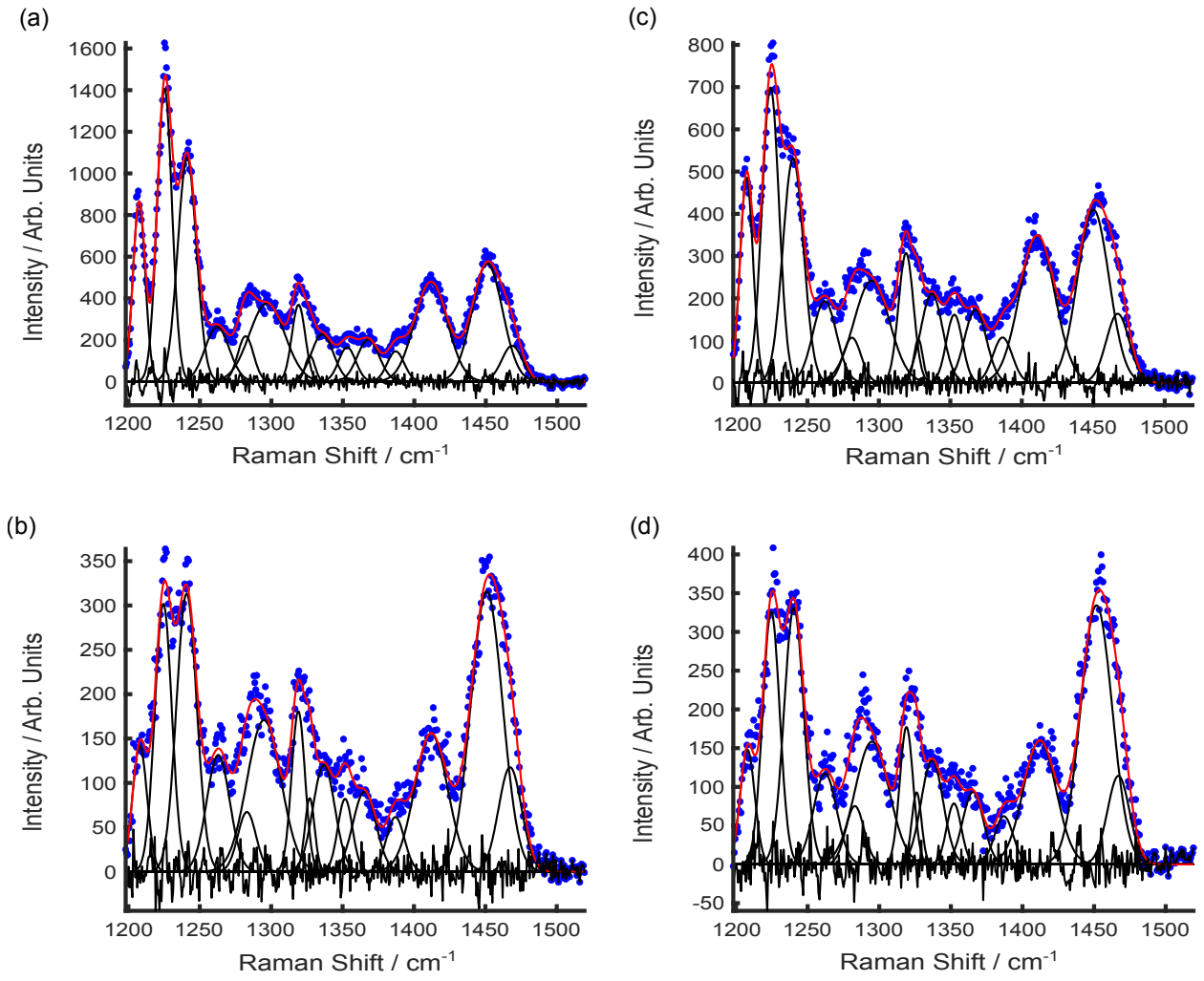

Figure S16: Deconvolution of amylin$_{20-29}$ polymorph 2 polarized Raman spectra for the Amide III region: (a) ZZ ($\chi^2_{red} = 1.8$), (b) ZX ($\chi^2_{red} = 1.5$), (c) XX ($\chi^2_{red} = 1.6$), and (d) XZ ($\chi^2_{red} = 1.7$).

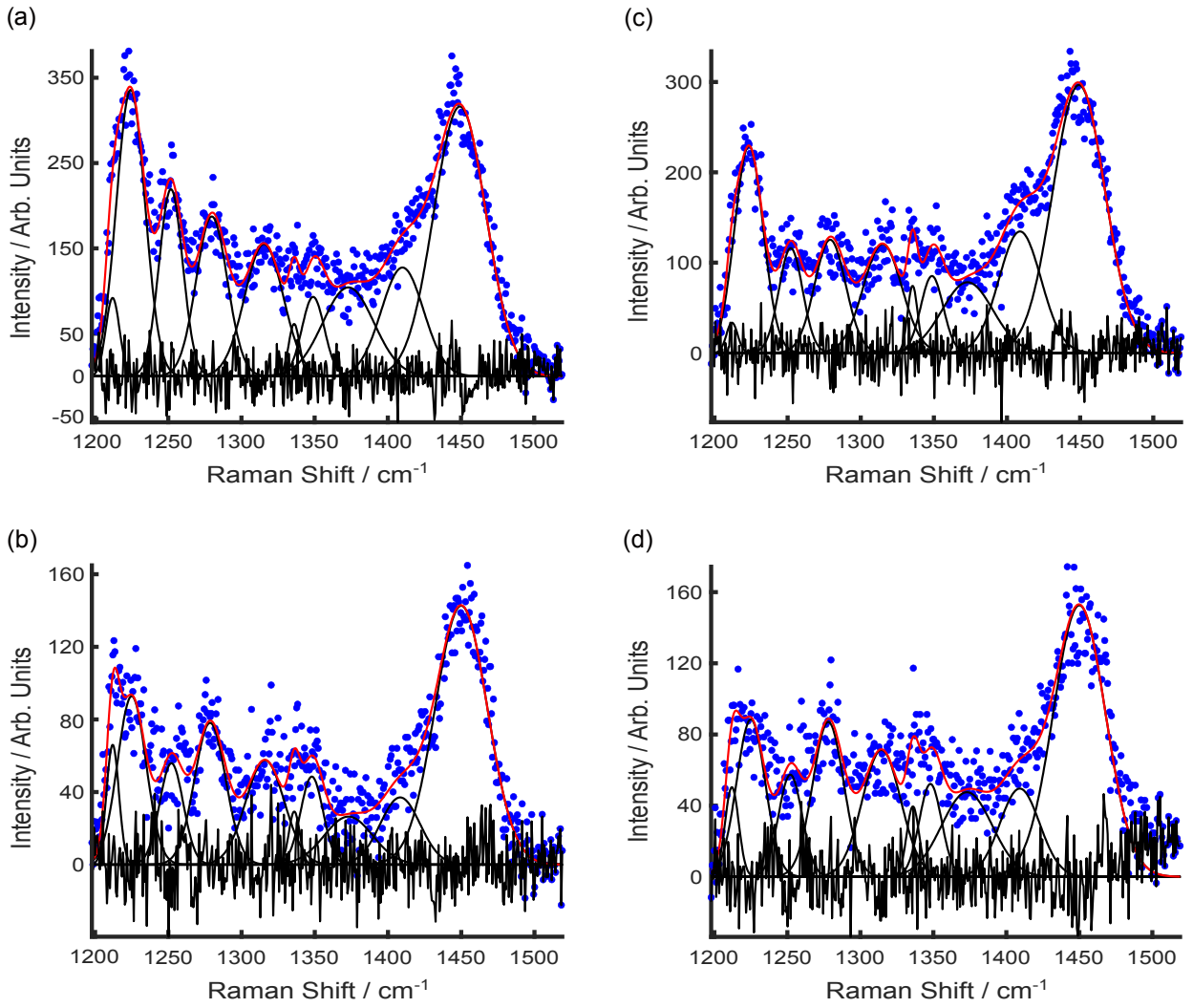

Figure S17: Deconvolution of Aβ_{25-35} fibrils polarized Raman spectra for the Amide III region: (a) ZZ ($\chi^2_{red} = 1.4$), (b) ZX ($\chi^2_{red} = 1.3$), (c) XX ($\chi^2_{red} = 1.3$), and (d) XZ ($\chi^2_{red} = 1.2$).

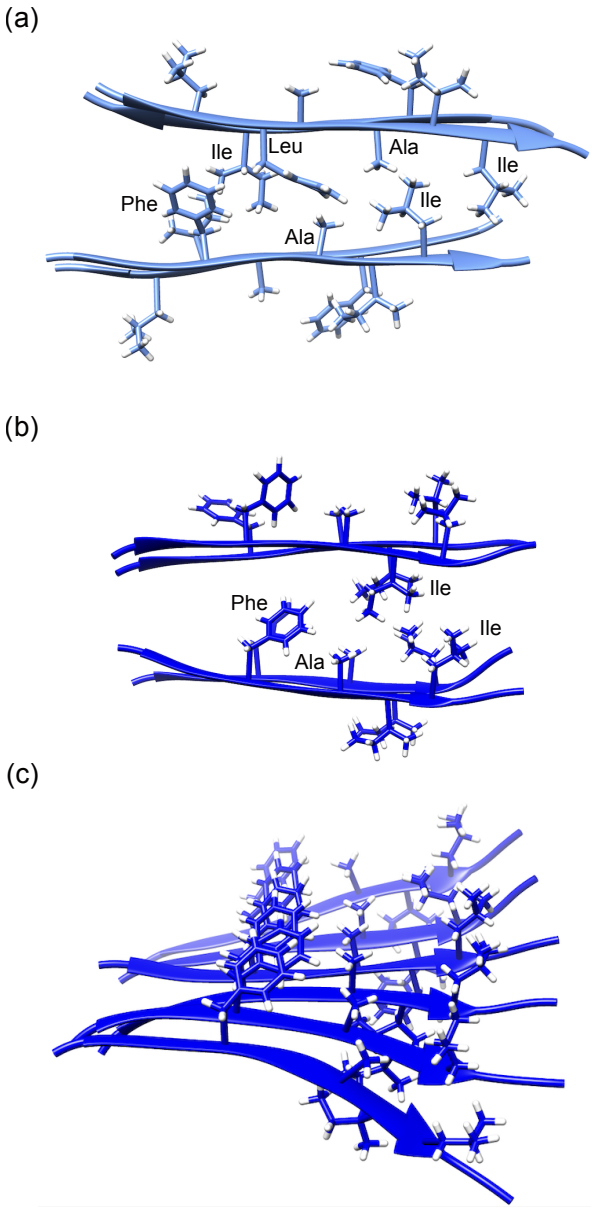

Figure S18: Structural snapshots showing amylin$_{20-29}$ polymorph 1 and 2 hydrophobic side chain interactions. (a) Amylin$_{20-29}$ polymorph 1 is comprised of antiparallel β-sheets with hydrophobic interactions between the side chains of Phe, Ala, and Ile residues within the same β-sheet, while the side chains of Leu, Ala, and Ile form hydrophobic zippers between β-sheets. (b,c) Amylin$_{20-29}$ polymorph 2 is comprised of parallel β-sheets with side chain interactions consisting hydrophobic and interactions with Phe, Ala, Ile, and Leu where Phe, Ala, Ile, and Leu residues aligned down the length of the β-sheets and π-stacking interactions with Phe and neighborking side chains. Ile, Leu, and Ala residues from opposite β-sheets additionally form hydrophobic zippers.

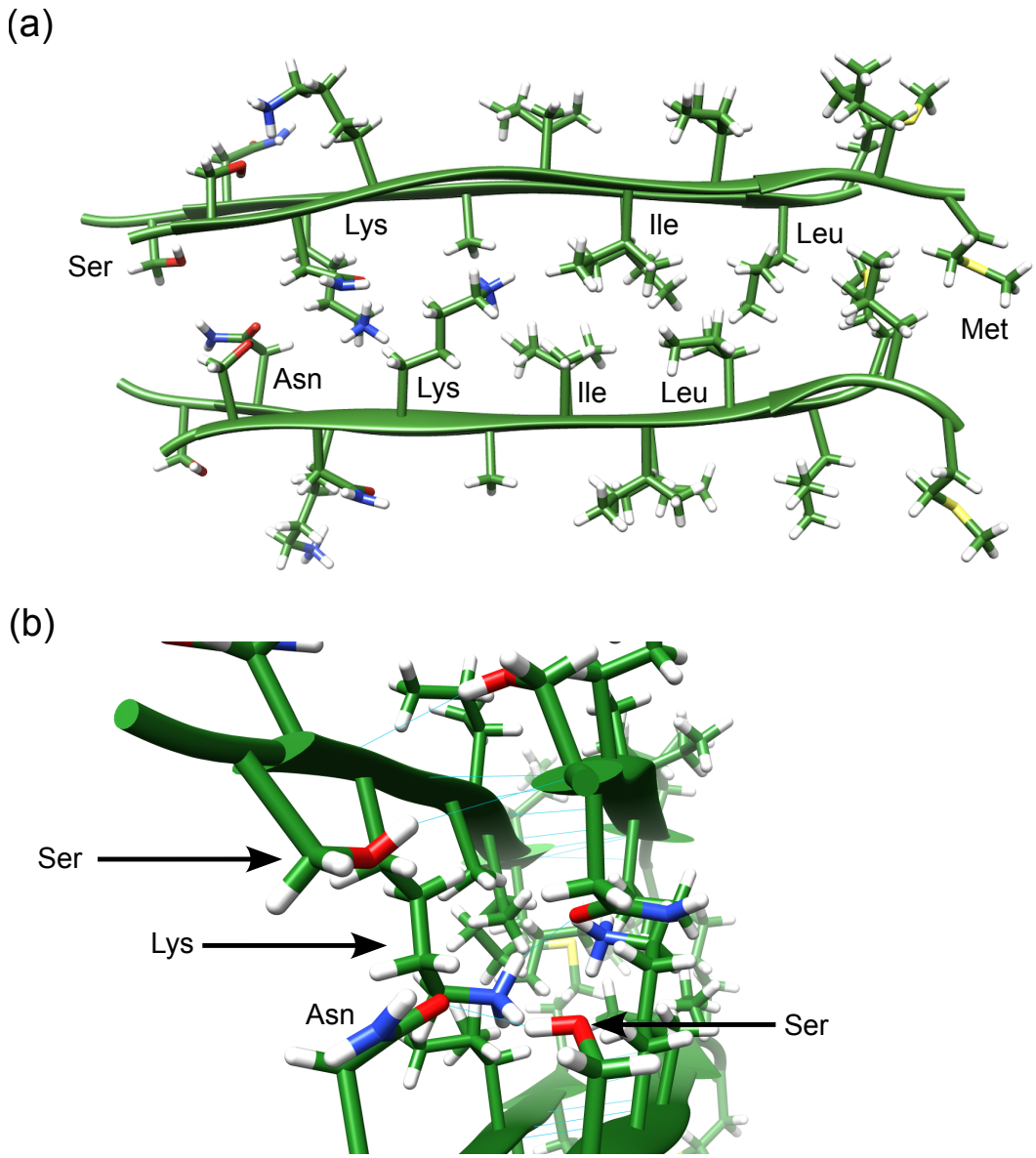

Figure S19: Structural snapshots showing Aβ_{25-35} fibrils side chain interactions. (a) Aβ_{25-35} fibril comprised of parallel β-sheets with hydrophobic side chain interactions. (b) Aβ_{25-35} fibril hydrogen bonding interactions between Ser, Asn, and Lys residues in neighboring β-strands.

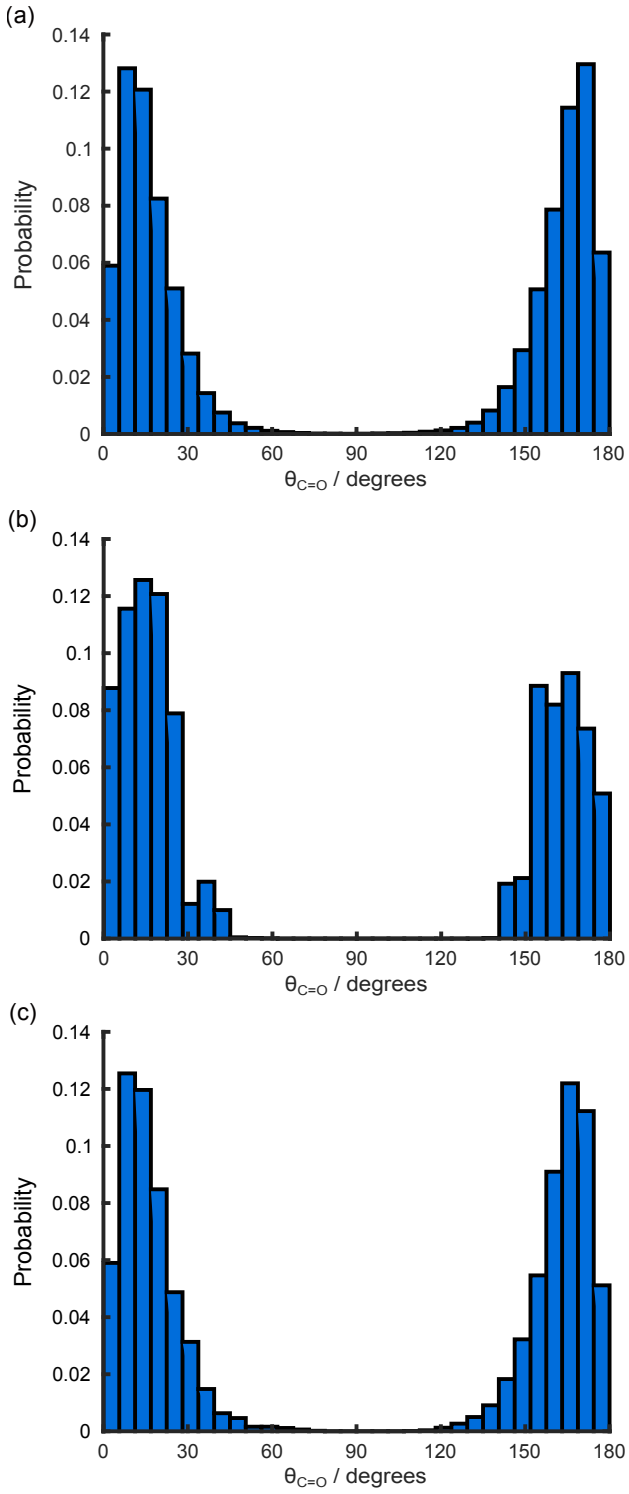

Figure S20: MD C=O distributions from unconstrained MD structures. (a) Amylin_{20-29} polymorph 1. (b) Amylin_{20-29} polymorph 2. (c) $\text{A}\beta_{25-35}$ fibrils.

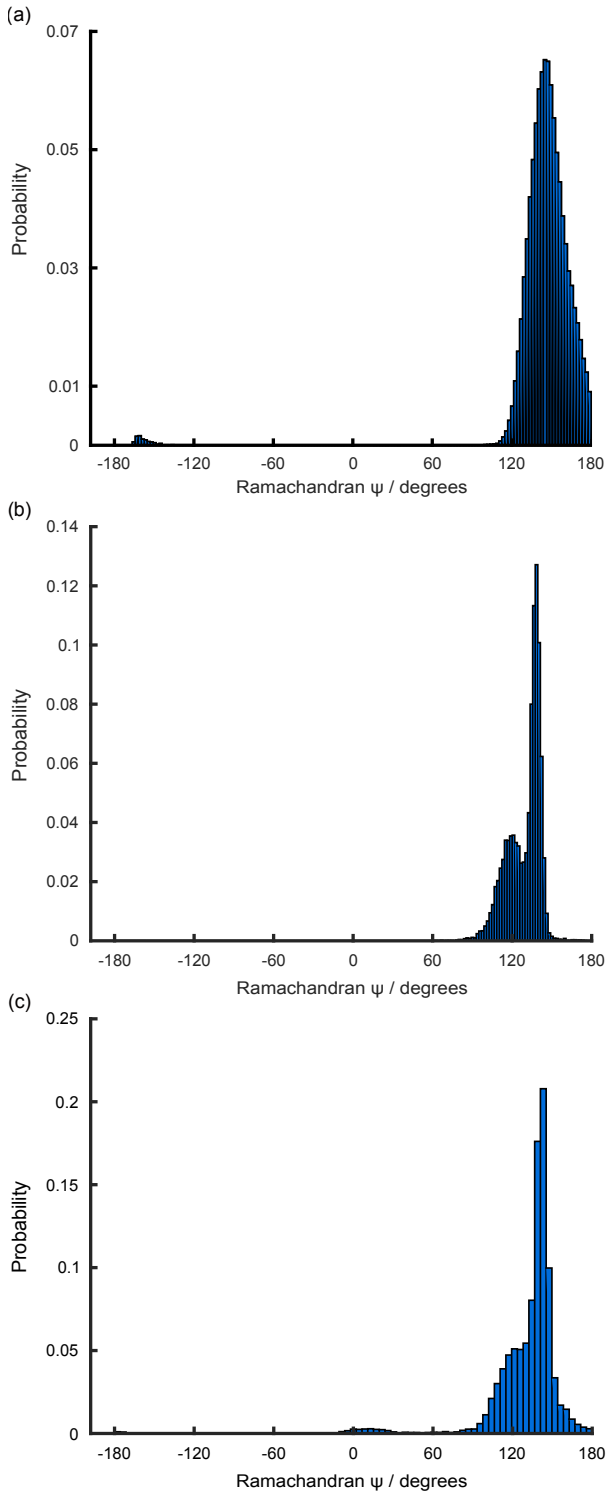

Figure S21: MD Ramachandran ψ-angle distributions from unconstrained MD structures. (a) Amylin$_{20-29}$ polymorph 1. (b) Amylin$_{20-29}$ polymorph 2. (c) Aβ_{25-35} fibrils.

References

(1) Mustafa, R.; Fitian, M.; Hamilton, N. B.; Li, J.; Silva, W. R.; Punihaole, D. *J. Phys. Chem. B.* **2022**, *126*, 8404–8414.

(2) Savitzky, A.; Golay, M. J. E. *Anal. Chem.* **1964**, *36*, 1627–1639.

(3) Asher, S. A.; Mikhonin, A. V.; Bykov, S. *J. Am. Chem. Soc.* **2004**, *126*, 8433–8440.

(4) Popova, L. A.; Kodali, R.; Wetzel, R.; Lednev, I. K. *J. Am. Chem. Soc.* **2010**, *132*, 6324–6328.

(5) Punihaole, D.; Workman, R. J.; Hong, Z.; Madura, J. D.; Asher, S. A. *J. Phys. Chem. B* **2016**, *120*, 3012–3026.

(6) Punihaole, D.; Jakubek, R. S.; Workman, R. J.; Marbella, L. E.; Campbell, P.; Madura, J. D.; Asher, S. A. *J. Phys. Chem. B* **2017**, *121*, 5953–5967.

(7) Labarthet, F. L.; Buffeteau, T.; Sourisseau, C. *Appl. Spectrosc.* **2000**, *54*, 699–705.

(8) Berne, B. J.; Pechukas, P.; Harp, G. D. *J. Chem. Phys.* **1968**, *49*, 3125–3129.

(9) Pottel, H.; Herreman, W.; van der Meer, B.; Ameloot, M. *Chem. Phys.* **1986**, *102*, 37–44.

(10) Bower, D. I. *J. Polym. Sci. Polym. Phys. Ed.* **1981**, *19*, 93–107.

(11) Rousseau, M.-E.; Lefèvre, T.; Beaulieu, L.; Asakura, T.; Pézolet, M. *Biomacromolecules* **2004**, *5*, 2247–2257.

(12) Koltun, W. L.; Waugh, D. F.; Bear, R. S. *J. Am. Chem. Soc.* **1954**, *76*, 413–417.